metals

MDPI

Article

Investigation of Welded Joints of Pipelines from an Existing Gas Transmission Network Exposed to Hydrogen—Part I: Structure, Mechanical Properties and Susceptibility to Hydrogen Embrittlement

Boris Yanachkov [1,2], Kateryna Valuiska [1], Yana Mourdjeva [1], Rumen Krastev [1,3,4], Vanya Dyakova [1,4], Tatiana Simeonova [1,3,4], Roumen H. Petrov [1,5], Krasimir Kolev [1,*], Margo Cauwels [2], Tom Depover [2] and Rumyana Lazarova [1,4]

1 Institute of Metal Science, Equipment, and Technologies with Center of Hydro- and Aerodynamics "Acad. A. Balevski" at the Bulgarian Academy of Sciences, 67 "Shipchenski prohod" Str., 1574 Sofia, Bulgaria
2 Department of Materials, Textiles and Chemical Engineering, Ghent University, 46 Technologiepark, 9052 Ghent, Belgium
3 Institute of Mechanics at the Bulgarian Academy of Sciences, Acad. Georgi Bonchev Str., Bl. 4, 1113 Sofia, Bulgaria
4 National Center for Mechatronics and Clean Technologies, 8 Kliment Ohridski Blvd., Building 8, 1756 Sofia, Bulgaria
5 Department of Electromechanical Systems and Metal Engineering, Ghent University, 46 Technologiepark, 9052 Ghent, Belgium
* Correspondence: kkolev@ims.bas.bg

Abstract

The utilization of hydrogen as a clean energy carrier requires an assessment of existing natural gas pipelines with respect to hydrogen embrittlement (HE). In this study, the structural integrity and hydrogen sensitivity of X52 (L360) pipeline steel from the Bulgarian gas transmission network after 31 years of service were investigated, focusing on production (longitudinal) and girth (circumferential) welded joints. Hydrogen content was measured in the base metal, production weld and girth weld before and after electrochemical charging, while in situ hydrogen charging during tensile testing was applied to simulate service conditions. Mechanical behavior was evaluated by tensile tests, and microstructural and fracture characteristics were analyzed by SEM and TEM. The results show significant spatial variations in hydrogen concentration, related to local microstructural heterogeneity and hydrogen trapping. In the as-operated state, fracture was localized mainly in the heat-affected zone. Hydrogen charging led to a pronounced reduction in ductility (approximately twofold), whereas yield and tensile strengths were only slightly affected. Failure analyses indicate a transition toward more brittle fracture mechanisms, dominated by quasi-cleavage and intergranular cracking in the as-charged state, with hydrogen embrittlement susceptibility indices demonstrating higher hydrogen sensitivity of the girth-welded joints.

Keywords: hydrogen embrittlement; pipeline steels; ferrite–pearlite steel; failure analysis; welds

Check for updates

Academic Editor: Alberto Campagnolo

Received: 20 February 2026
Revised: 23 March 2026
Accepted: 28 March 2026
Published: 31 March 2026

Copyright: © 2026 by the authors. Licensee MDPI, Basel, Switzerland. This article is an open access article distributed under the terms and conditions of the Creative Commons Attribution (CC BY) license.

1. Introduction

The use of hydrogen as a clean energy carrier is a promising approach that can be implemented either by utilizing the existing natural gas transmission network or by

constructing new infrastructure specifically designed for hydrogen storage and transport. From an economic perspective, repurposing the existing natural gas pipeline network is advantageous. However, such infrastructure must be thoroughly tested for hydrogen-related effects and evaluated in terms of its suitability for hydrogen transportation.

Carbon and low-alloy steels are commonly used materials for gas pipelines. Depending on their chemical composition and microstructural characteristics, these steels exhibit varying degrees of susceptibility to hydrogen embrittlement (HE). Hydrogen embrittlement is a process in which hydrogen atoms penetrate the material in a hydrogen-containing environment, leading to a significant reduction in mechanical strength and ductility, and therefore to increased brittleness [1].

Previous studies [2–6] have shown that high-strength pipeline steels, such as X80 and X100, exhibit greater susceptibility to hydrogen embrittlement compared to low- and medium-strength steels, such as X42 and X52. In line with these findings, standards such as ASME B31.12 "Hydrogen Piping and Pipelines" [7] and the European Compressed Gas Association CGA G-5.6 (2005, R2013) "Hydrogen Pipeline Systems" recommend the use of medium- and low-strength pipeline steels for hydrogen transportation applications [8–10].

The pipes from the Bulgarian gas transmission network investigated in the present study are manufactured from a high-strength low-alloy structural steel intended for general-purpose constructions with welded, bolted, and riveted joints. The closest European equivalent of this steel is X52, which corresponds to grade L360 according to the international standard ISO 3183 [11]. Newly obtained important data on how X52 steel, produced before 31 years and used in natural gas transportation, behaves in hydrogen environments could be useful in the design of the steels and pipelines for hydrogen transmission, and especially for determining the requirements for their exploitation, which is the purpose of the relevant standards, such as the current ones ASME B31.8 [12] and ASME B31.12 [7].

Literature data indicate that the susceptibility of pipeline steels to hydrogen embrittlement depends on factors such as chemical composition, phase composition (particularly the presence of inclusions), microstructural characteristics, and stress state [13–16]. Zhang et al. [17] reported that the accumulation of high-density dislocations in elongated ferrite bands within bainitic regions of the microstructure increases the susceptibility of upper bainite to hydrogen embrittlement compared to polygonal ferrite and acicular ferrite. Similarly, ref. [18] demonstrated that microstructures consisting of acicular ferrite and spheroidized pearlite exhibit greater resistance to hydrogen embrittlement than those composed of polygonal ferrite and spheroidized pearlite. These observations indicate that different phases and microstructural constituents exhibit varying sensitivity to hydrogen embrittlement.

Exposure to hydrogen has a particularly significant impact on gas pipelines containing weld seams, as these represent critical structural elements. Due to their small size and high mobility, hydrogen atoms readily diffuse into the steel lattice and accumulate at microstructural defects commonly found in welds, such as grain boundaries, slag inclusions, and existing microcracks. This accumulation deteriorates mechanical properties, including ductility and fracture toughness, thereby increasing the risk of brittle failure.

Welding induces significant residual stresses in the metal, which, under hydrogen charging, may change both in magnitude and distribution, including the transformation of compressive stresses into tensile stresses in the transition zones between the weld seam and the heat-affected zone, and especially between the heat-affected zone and the base metal. This promotes crack initiation and propagation in these regions [19,20].

The heat-affected zone (HAZ) undergoes thermal cycles during multiple welds, which result in microstructures that are different from those of the base metal. This makes this region particularly susceptible to hydrogen-induced cracking. The effect of hydrogen on

the metal is often combined with other factors, such as mechanical loading, corrosion, and low-temperature operating conditions, thereby increasing the overall complexity of studying metal degradation processes and failure mechanisms.

In a gas pipeline that has been in service for approximately 31 years, hydrogen may be present both in a mobile (diffusible) state and in a trapped form, with its distribution being strongly heterogeneous and dependent on the local microstructure and stress state [21]. A portion of the hydrogen exists as lattice-dissolved hydrogen occupying interstitial sites in the ferritic crystal lattice. This fraction exhibits high mobility at room temperature and plays a key role in hydrogen embrittlement processes, as it can redistribute toward regions of high stress [22]. Another portion of the hydrogen is trapped, being localized at various microstructural defects such as dislocations and dislocation pile-ups, grain and subgrain boundaries, ferrite–cementite interfaces within pearlitic colonies, carbide particles, non-metallic inclusions, as well as microcracks and pores formed during long-term service.

In the base material of the pipe, which typically exhibits a ferritic–pearlitic or bainitic microstructure, hydrogen predominantly accumulates in regions with increased defect density generated as a result of prolonged exposure to operating pressure, temperature fluctuations, and corrosion processes. Service loading promotes dislocation multiplication and localized plastic deformation, thereby increasing the number of potential trapping sites. In the vicinity of the internal pipe surface, corrosion-induced defects may further contribute as preferential hydrogen accumulation sites. A characteristic feature of gas pipeline pipes is the presence of two types of welded joints: a production weld and a girth weld. The seam, formed during pipe production, contains a HAZ in which the microstructure differs from that of the base material. These regions often exhibit coarser grains, increased dislocation density, and the possible formation of harder microstructural constituents. Such features lead to a higher density of hydrogen trapping sites and create conditions for localized hydrogen accumulation [23].

Gas pipelines have two types of weld seams: a longitudinal production weld (PW), which is performed automatically at the production plant, and a circumferential girth weld (GW), which is carried out directly during pipe installation in the pipeline system. The girth weld, produced during on-site joining of individual pipe sections, is typically characterized by greater structural heterogeneity, a multilayer weld structure, and elevated residual stresses. The combination of residual stresses, metallurgical transformations within the heat-affected zone, and potential microdefects renders this region particularly susceptible to hydrogen accumulation and to the initiation of hydrogen-induced cracking [24].

The type of weld seam used in pipes depends on the diameter, wall thickness, and the operating environment in which the pipe will be used. In the welding of steel pipes, iron-based electrodes alloyed with elements such as manganese (Mn) and silicon (Si) are most commonly applied. The electrode coating is typically rutile, basic, or cellulosic. In automatic and submerged arc welding, fluxes based on silicon dioxide (SiO_2), calcium fluoride (CaF_2), and aluminum oxide (Al_2O_3) are used to stabilize the arc and protect the molten metal from oxidation [25]. The resistance of the welded joint to hydrogen effects largely depends on the quality with which the welding procedure is performed.

The weld seam is usually the weakest part of gas pipelines, and long-term safe operation depends on its defect-free condition and strength. These considerations highlight the need for a detailed investigation of the microstructure and mechanical properties of welded joints in order to assess their susceptibility to hydrogen embrittlement and to identify the dominant failure mechanisms.

In [26], the susceptibility to hydrogen embrittlement of the two types of welds—the longitudinal made by submerged arc welding (SAW), and girth made by inert-gas welding

(TIG)—was thoroughly investigated. Valuable results were obtained there, but since they do not refer to a pipe operated for many years in real conditions and since it is only assumed that the sensitivity to HE of different microstructures in a weld depends mainly on the differences in the grain boundary structures, we believe that it is necessary to continue the detailed investigation of the microstructure and mechanical properties of welded joints to assess their susceptibility to hydrogen embrittlement and to identify the dominant failure mechanisms. Considerably less attention has been devoted to the potential spatial heterogeneity of hydrogen in pipelines after long-term service, as well as to the influence of this initial hydrogen distribution on its subsequent evolution during charging and on the response of different regions within welded joints. This research approach has been adopted in the present study.

The aim of the present work arises from the need to assess the suitability of the Bulgarian gas transmission network, after 31 years of service, for hydrogen transportation. Therefore, the objective of the first part of this study is to investigate the microstructure and mechanical properties of specimens containing two types of welds, both after 31 years of operation and after additional hydrogen charging.

It should be noted that the present results are case-specific for the investigated pipeline steel after 31 years of service and should not be interpreted as representative of a general trend in hydrogen trapping behavior or embrittlement susceptibility for pipeline steels with different service histories.

2. Methodology

2.1. Materials

Natural gas pipelines made of X52 steel from the existing transmission system in Bulgaria, with an outer diameter of 1020 mm and a wall thickness of 10 mm, were investigated. The pipes had been in service for 31 years.

The chemical composition of the base metal (BM), the PW, and the GW of the pipe were determined using an optical emission spectrometer (Q4 95 TASMAN Q101750-C130, BRUKER AXS, Berlin, Germany). The results are presented in Table 1.

Table 1. Chemical composition (in wt.%) of the investigated pipeline steel in the BM, PW, and GW.

	C	Si	Mn	S	P	Cr	Cu	Ni
BM	0.133	0.48	1.30	0.016	0.014	0.02	0.07	0.03
PW	0.111	0.66	1.46	0.016	0.017	0.26	0.08	0.075
GW	0.092	0.43	1.03	0.011	0.019	0.04	0.06	0.04

The measured element concentrations comply with the API 5L X52 pipeline standard. Figure 1 shows a schematic representation of the location of the two types of welded joints (PW and GW) on the pipe. Images of the macrostructure of both welds are also presented in the same figure. The welds have symmetrical geometry and are free of macroscopic defects. Since it is necessary for the welded zone to be located in the middle of the working section of the tensile specimens, the specimens have different orientations relative to the longitudinal axis of the pipe.

Five specimens were tested for each condition and each region (BM, PW, and GW) in both the uncharged and hydrogen-charged states.

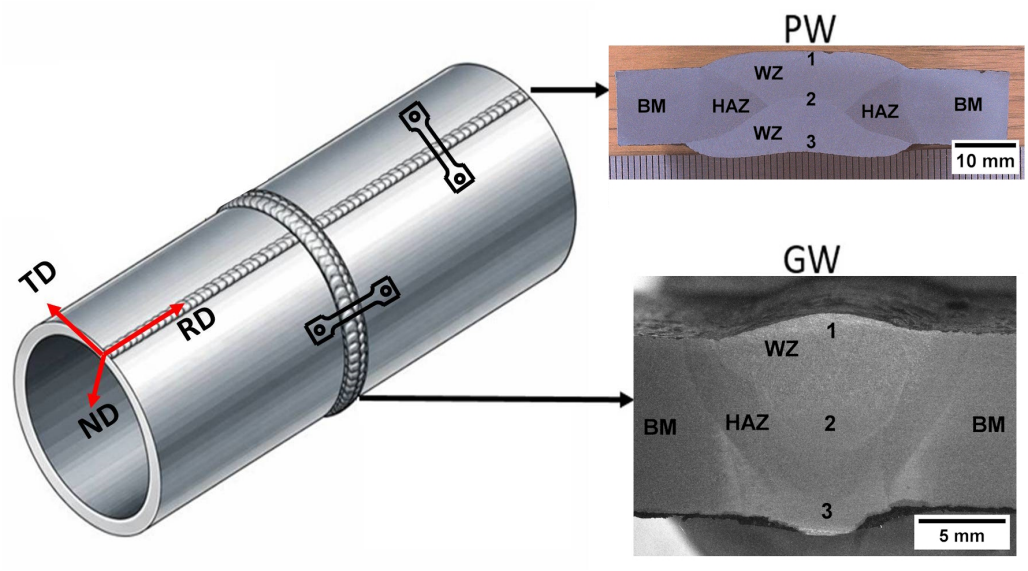

Figure 1. A schematic representation of the sampling places and orientations of the PW and GW specimens, relative to the gas pipeline. The abbreviations RD, TD and ND correspond to the plate rolling direction, transverse and normal direction, respectively.

2.2. Test Methods

2.2.1. Hydrogen Concentration Measurement

The hydrogen concentration in the investigated pipeline steel was quantitatively determined both in the initial condition and after electrochemical charging, in order to establish a reliable basis for interpreting the results of subsequent mechanical testing. Prior to additional hydrogen charging or mechanical loading, the initial hydrogen content was determined using the total extraction method by melting.

The tested specimens were taken from three characteristic regions of the pipeline, namely the base material, the longitudinal production weld seam, and the circumferential girth weld seam. Samples with dimensions of 0.5 × 6 × 8 mm were extracted from the pipe exclusively by mechanical cutting under sufficient cooling conditions. This precaution was taken to ensure accurate measurement of the hydrogen concentration in the initial material. Extraction was performed using a G8 GALILEO apparatus (Bruker, Berlin, Germany), employing a pulsed graphite furnace connected to a thermal conductivity detector.

In order to determine how the properties of the welded joints change with increasing hydrogen concentration, an electrochemical charging technique was employed. In the same manner as for the initial hydrogen concentration measurement, specimens with identical geometry were extracted from the same regions of the pipe. During this test, the specimens were subjected to hydrogen charging in a 0.5 M H_2SO_4 solution at a current density of 5 mA/cm^2 for a period of 1 h. After charging, the hydrogen content was measured using the same method.

2.2.2. Tensile Testing Under In Situ Hydrogen Charging

In order to achieve the most accurate possible representation of the service conditions of pipeline steel in a hydrogen-rich environment, an in situ hydrogen charging technique was applied during mechanical testing. This method involves the use of a cell, described in further detail in our previous work [27], in which the specimen is mounted and charged with hydrogen from a 0.5 M H_2SO_4 electrolyte. In a comparative study [28] and in our previous work [27], it was demonstrated that the selected charging parameters are sufficient to introduce hydrogen into the specimens without inducing internal cracking or surface blistering. Furthermore, as discussed in Section 3.2 (“Hydrogen con-

centration"), the measured hydrogen concentrations obtained using an electrolyte of 0.5 M H_2SO_4 without additional promoters show good agreement with the values reported in our previous study.

The specimen–cell assembly is mounted on a mechanical testing machine HA 250 (ZWICK ROELL, Ulm, Germany). All tests are carried out at a constant strain rate of 1×10^{-4} s^{-1} under simultaneous electrochemical hydrogen charging.

2.3. Characterization Methods

The microstructure of the steel in the tested specimens after hydrogen charging and tensile testing was characterized using scanning electron microscopy (SEM) and transmission electron microscopy (TEM). Fractographic analysis was performed on the fracture surfaces along the tensile loading direction. The cross-sectional dimensions of the specimens prior to fracture were 6 mm in width and 0.5 mm in thickness.

Additional investigations were carried out on the flat part of the specimens after grinding, polishing, and etching with 2% nital, in order to detect and examine the formation and propagation of pores and cracks in the region located directly beneath the fracture surface. This region is characterized by increased local stress concentration and intensive plastic deformation, leading to pore nucleation and coalescence, as well as the formation of microcracks. The observations were performed using a HIROX 5500 scanning electron microscope (HIROX Europe, Limonest, France), equipped with a BRUKER EDXS system (BRUKER Co., Berlin, Germany). Areas differing in fracture characteristics were measured, and their relative fractions with respect to the total fractured surface area were calculated.

TEM analysis was conducted using a JEM 1011 microscope (JEOL Ltd., Tokyo, Japan) at an accelerating voltage of 100 kV. The specimen foils were prepared on TENUPOL 5 (STRUERS Ltd., Copenhagen, Denmark) at voltage 45 V, temperature 5 °C, and at flow rate setting of 20, with electrolyte "A2". The observation plane of the TEM specimens was normal to ND of the plate.

3. Results and Discussion

From the micrographs in Figures 2 and 3, a wide variety of microstructures formed at different locations within the welded joints can be observed. This structural heterogeneity in the joint region makes it susceptible to defect initiation. Moreover, it creates different conditions for hydrogen diffusion and trapping at various points of the welded joint, which further identifies this area as critical.

3.1. Structure Analysis in the Initial State

The microstructure of the base metal of the production weld consists of large equiaxed polygonal ferrite (PF) grains and pearlite (P) colonies filling the volume of the former austenite grains—Figure 2a. The microstructure of the HAZ represents large, relatively equiaxed ferrite grains and pearlite colonies, most of which are located along the boundaries of the former austenite grains—Figure 2b. The microstructure at point 1 seems to be a mixture of PF, pearlite and lath bainite (LB) [29]—Figure 2c. Acicular ferrite (AF) and carbide precipitates compose the microstructure at point 2—Figure 2d. PF, carbide precipitates, and LB are seen at point 3—Figure 2e.

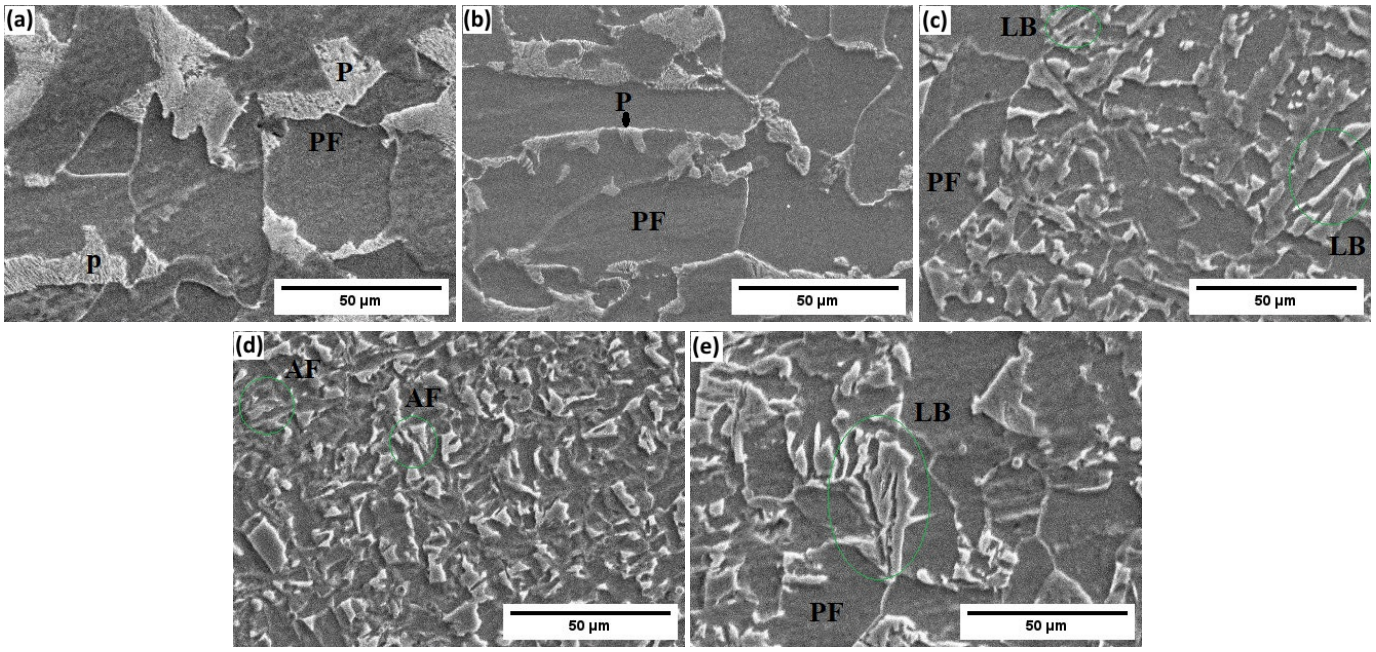

Figure 2. Microstructure of the production weld: (**a**) base metal next to the weld; (**b**) HAZ; (**c**–**e**) microstructures of weld seam at different locations (1, 2, and 3 respectively from Figure 1).

The microstructure of the base metal of the girth weld consists of large equiaxed polygonal ferrite grains and pearlite colonies filling the volume of the former austenite grains—Figure 3a. The microstructure of the HAZ consists predominantly of AF and carbide precipitates—Figure 3b. The microstructure at point 1 consists predominantly of AF and LB—Figure 3c. PF, AF and LB are seen at point 2—Figure 3d. Equiaxed polygonal ferrite grains and pearlite colonies filling the volume of the former austenite grains compose the microstructure at point 3—Figure 3e.

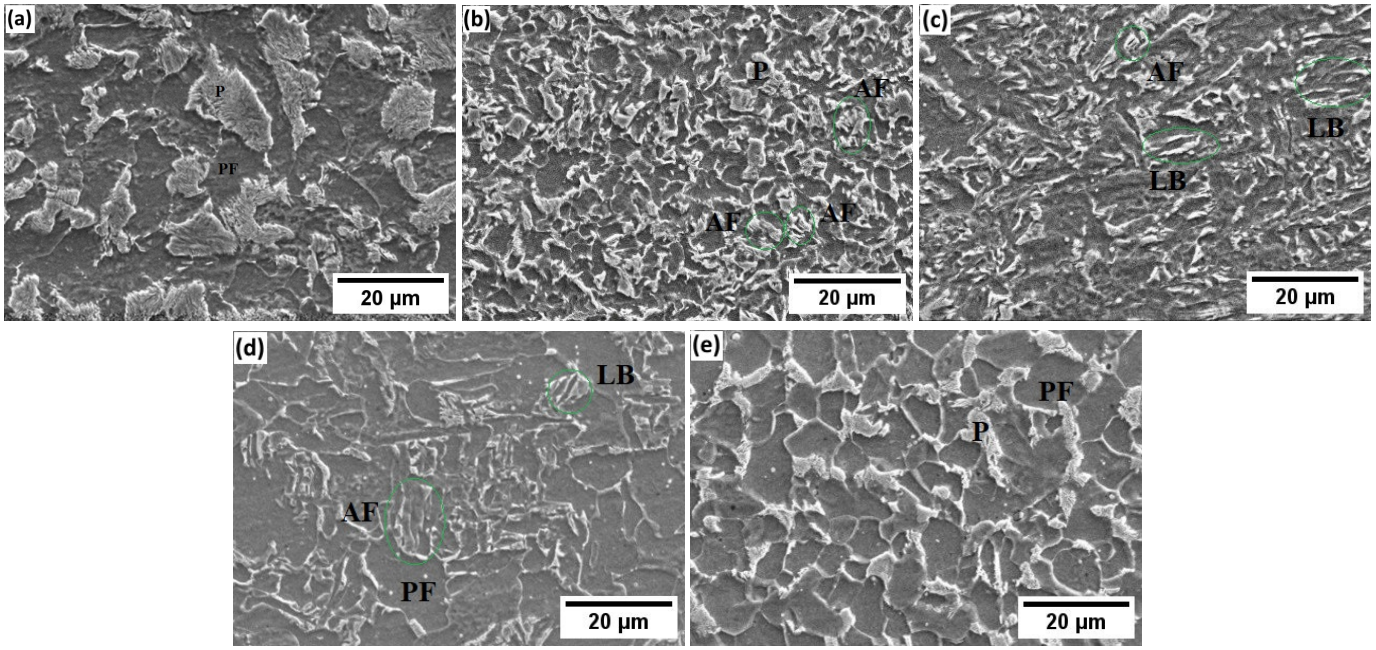

Figure 3. Microstructure of the girth weld: (**a**) base metal next to the weld; (**b**) HAZ; (**c**–**e**) microstructures of weld seam at different locations (1, 2, and 3 respectively from Figure 1).

PF, LB and a small amount of granular bainite are seen at point 2—Figure 3d. Equiaxed ferrite grains and pearlite colonies filling the volume of the former austenite grains compose the microstructure at point 3—Figure 3e.

3.2. Hydrogen Concentration

Despite originating from the same pipeline segment, the measured hydrogen concentrations in the as-received condition were not identical (Table 2), indicating that hydrogen retention is strongly governed by local microstructural features and defect populations rather than representing a uniform bulk property of the pipeline steel.

Table 2. Measured hydrogen concentrations in the different regions of the investigated pipeline in the initial state and after electrochemical hydrogen charging.

	BM, wppm	PW, wppm	GW, wppm
Initial state	1.13 ± 0.2	1.57 ± 0.44	2.9 ± 0.5
After electrochemical charging	4.05 ± 0.13	2.11 ± 0.31	5.25 ± 1.02

After electrochemical charging, a different distribution and ratio of hydrogen concentrations among the investigated regions were observed. These findings suggest that long-term service leads to the development of region-specific hydrogen-trapping characteristics, which may significantly change under short-term hydrogen exposure or increased hydrogen uptake.

3.3. Tensile Testing

The results of the tensile tests for specimens before hydrogen charging (BM, PW, and GW) and after in situ hydrogen charging (PW-H, GW-H, and BM-H) are summarized in Figure 4. Figure 4a shows the average values of the strength parameters—the yield strength ($R_{p0.5}$) and the ultimate tensile strength (R_m). Figure 4b presents the average values of the ductility parameters—the uniform elongation at maximum force (A_g) and the total elongation at fracture (A_t).

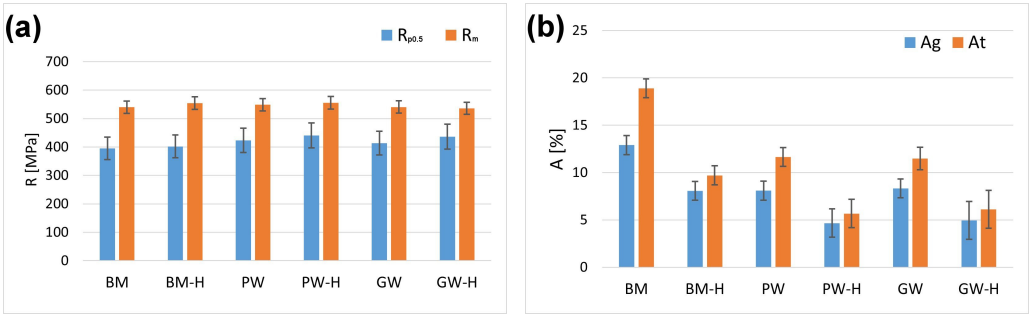

Figure 4. Data on the average values of the mechanical properties of welded-joint specimens after 31 years of service and after additional in situ hydrogen charging: (**a**) strength characteristics: yield strength ($R_{p0.5}$) and tensile strength (R_m); (**b**) ductility characteristics: A_g—percentage plastic extension at maximum force, and A_t—total elongation at fracture.

The strength characteristics of specimens with and without welded joints show similar values (Figure 4a). After long-term service, the difference in yield strength ($R_{p0.5}$) between the BM specimens, those containing PW, and those containing GW does not exceed 10%, while the difference in tensile strength (R_m) is approximately 4%. Hydrogen charging does not significantly affect the strength properties of the tested specimens; the observed increase in strength parameters is limited to approximately 2–4%.

In contrast, the ductility values of the base metal specimens and those containing girth or production welds differ (Figure 4b). The highest ductility is observed in the BM specimen. Additional hydrogen charging leads to an approximately twofold reduction in ductility (A_g and A_t) for all types of specimens, i.e., they become more brittle than uncharged specimens (Figure 4b).

3.4. Microstructure of Tensile-Fractured Specimens in the Area Beneath the Fracture Surface (ABFS) Before and After Hydrogen Charging

The microstructural analysis of the region immediately beneath the fracture surface (cross-sectional area beneath fracture surface—ABFS [30]) is over a wide range of about 400 µm. It provides information on which part of the welded joint—the weld metal (PW or GW), the HAZ, or the BM—the fracture occurred. In addition, this analysis allows the assessment of the nature of local plastic deformation, as well as the type, distribution, and morphology of the formed defects (pores, cracks, microvoids, etc.) and their interaction with the microstructural constituents. By comparing these characteristics in non-hydrogen-charged and hydrogen-charged specimens containing PW and GW, the influence of hydrogen content on the mechanical behavior of the steel under tensile loading can be evaluated.

3.4.1. Non-Hydrogen-Charged Specimen Containing GW

Figure 5a,b shows the microstructure in the ABFS of a non-charged specimen containing a GW. Relatively small and non-equiaxed grains are observed, the boundaries of which correspond to prior austenite grains transformed into a ferrite–pearlite structure. This morphology suggests that the observed zone belongs to the HAZ, and the fracture most likely occurred in this area. The relatively lower pearlite content in this zone can be associated with local carbon depletion during the welding thermal cycle, which could lead to lower local strength of the material. The grain morphology reflects non-equilibrium thermal conditions during welding and can be associated with the presence of residual stresses. The combination of locally reduced strength and possible residual stresses in the HAZ probably contributed to the initiation of the fracture in this zone.

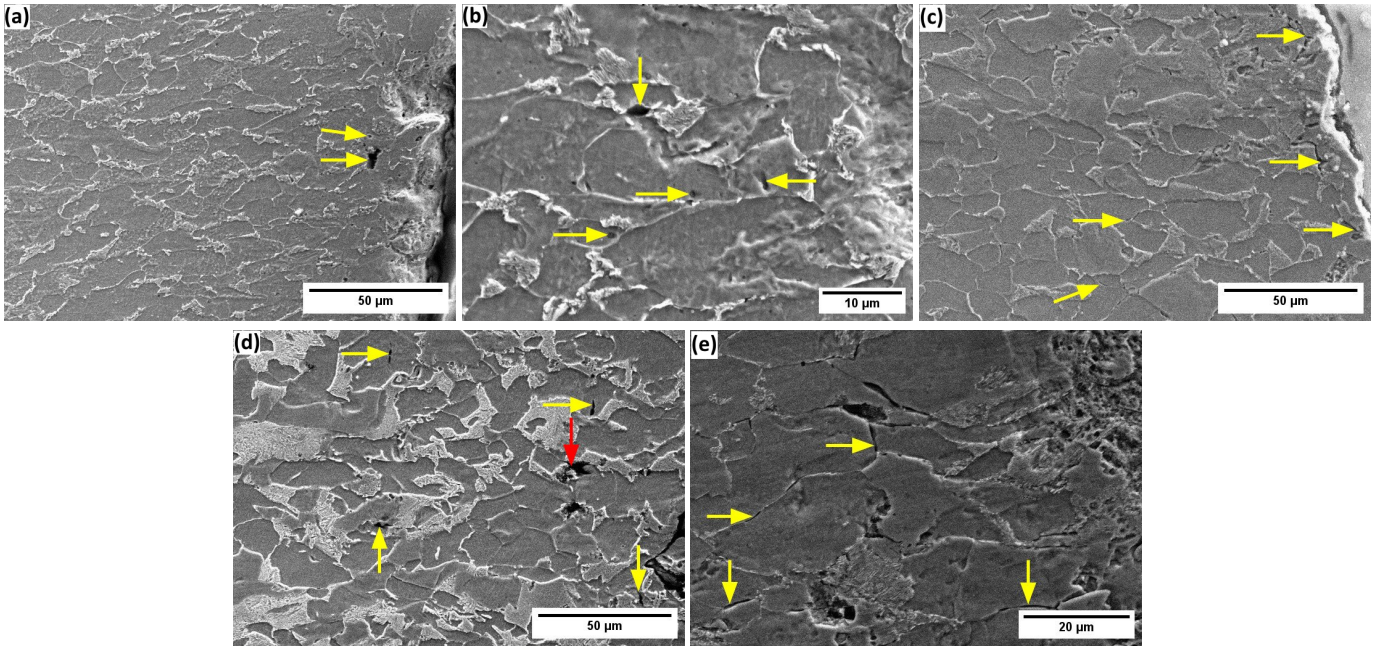

Figure 5. Microstructure in the area below the fracture surface (ABFS) of the initial specimens: (**a**,**b**) specimen containing GW, and (**c**–**e**) specimen containing PW.

3.4.2. Non-Hydrogen-Charged Specimen Containing PW

Figure 5c–e show the microstructure in the ABFS of a non-hydrogen-charged specimen containing a PW, which also fractured within the HAZ during tensile testing. In the two marginal regions of the ABFS (Figure 5c,e), an extremely low pearlite content is observed, which can be explained by local carbon depletion due to carbon redistribution during the welding process. In these regions, cracks along grain boundaries are detected, i.e., intergranular fracture (Figure 5e).

In the central region of the ABFS (Figure 5d), located close to the base metal and characterized by a higher pearlite content, cracks within ferrite grains, microvoids in the ferritic matrix, microvoids at pearlite colony boundaries, and isolated cracks within pearlite colonies (red arrow) are observed. Due to the isolated occurrence of cracks in pearlite colonies, these features can be considered atypical for damage in non-hydrogen-charged specimens.

In both non-hydrogen-charged specimens (containing GW and PW), fracture occurred in the HAZ. This suggests that welding thermal cycles create structural conditions that increase the susceptibility of this zone to fracture.

3.4.3. Hydrogen-Charged Specimen Containing GW

Figure 6a–d present the microstructure in the ABFS of a hydrogen-charged specimen containing a GW. In addition to relatively equiaxed grains, elongated fine cementite formations are observed, reflecting more non-equilibrium conditions during structure formation—Figure 6a. These features suggest that the analyzed region is located within or near the HAZ.

In this region, cracks and microvoids are most frequently observed within the ferrite grains (yellow arrows), but also within the pearlite colonies (red arrows). The fracture of pearlite colonies is atypical for non-hydrogen-charged specimens; therefore, the appearance of cracks in these regions in the hydrogen-charged specimen can be interpreted as a manifestation of hydrogen-assisted damage. Such behavior is consistent with known mechanisms of hydrogen-induced degradation in ferrite–pearlite steels, such as HELP (Hydrogen-Enhanced Localized Plasticity) and HEDE (Hydrogen-Enhanced Decohesion) [31].

In Figure 6c, an orientation-distinct band containing cementite lamellae aligned approximately parallel to the fracture surface is observed. This band was most likely formed during the solidification of the molten metal in the direction of heat flow during welding. Between this oriented region and the surrounding equiaxed ferrite grains, a large crack is detected, along with additional smaller cracks and pores. The different orientation and morphology of adjacent microstructural regions indicate structural heterogeneity, which may act as a local stress concentrator and promote defect formation.

In the same specimen, regions containing numerous spherical non-metallic inclusions detached from the metallic matrix are also observed (Figure 6d marked with green arrows). Due to their rounded shape, these inclusions do not represent strong stress concentrators and do not directly initiate cracks. However, local cracks and microvoids are observed around some of them (Figure 6e). It is well known that non-metallic inclusions act as hydrogen traps in steel, and the high density of their distribution in this region evidently facilitates metal degradation processes.

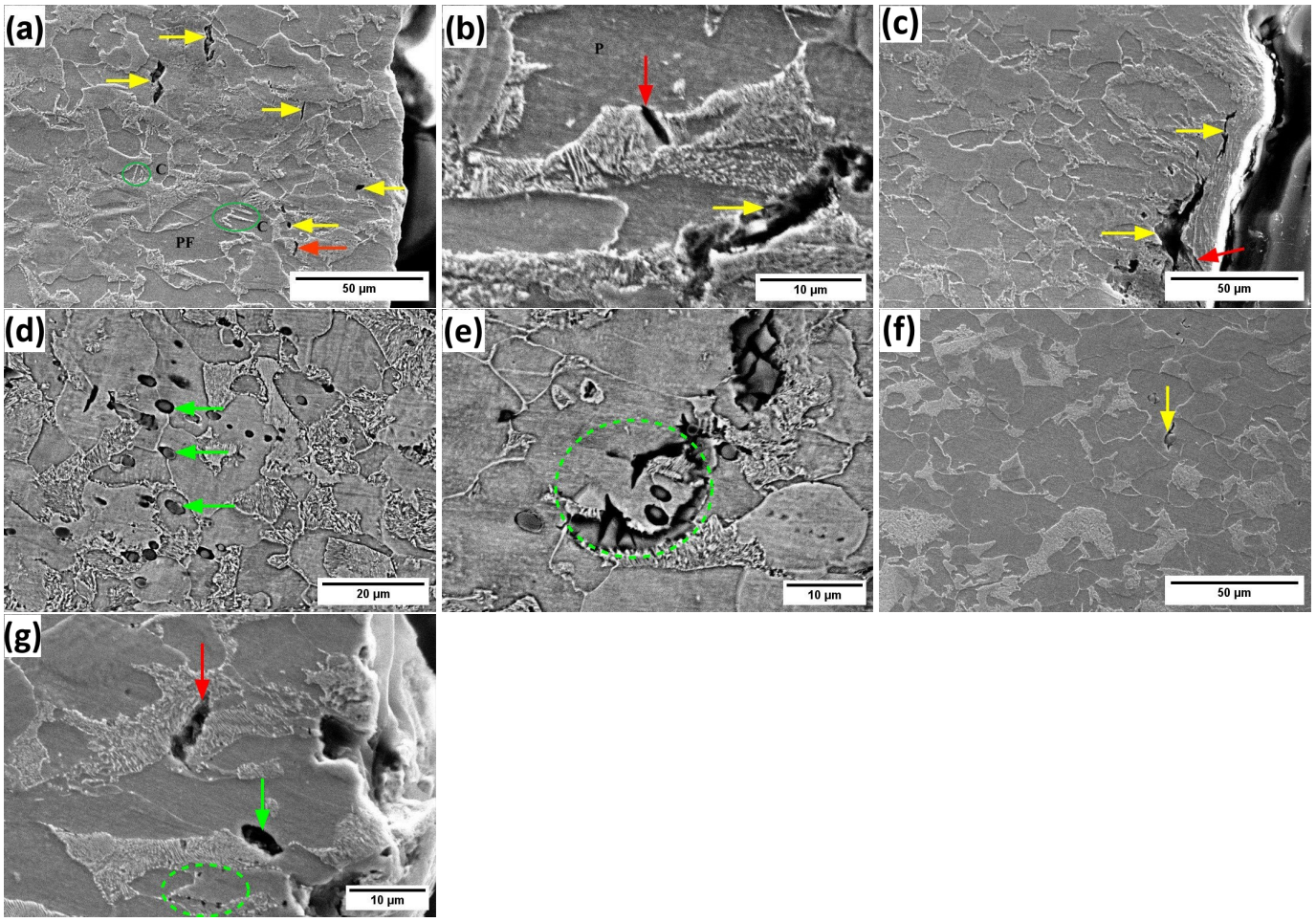

Figure 6. Microstructure in the ABFS of the specimens after hydrogen charging: (**a**–**e**) specimen containing GW; (**f**,**g**)—specimen containing PW.

3.4.4. Hydrogen-Charged Specimen Containing PW

Figure 6f,g show the microstructure in the ABFS of a hydrogen-charged specimen containing a PW, in which failure occurred in the HAZ immediately adjacent to the BM. Similar to the uncharged specimen containing GW, cracks and microvoids are observed both within the ferrite grains and within the pearlite colonies. The nature and localization of these defects, as well as the fact that the fracture is shifted from the HAZ to the base metal, can be interpreted as an indication of a hydrogen-assisted fracture mechanism.

It should be noted that the interpretation of the observed defects as hydrogen-related is based on comparative microstructural analysis between hydrogen-charged and non-hydrogen-charged specimens, without direct quantitative determination of hydrogen content.

3.5. Fractographic Analysis

The fracture surfaces of the PW and PW-H specimens, taken from the mid-thickness of the pipe wall after tensile testing in the initial state and after additional hydrogen charging, are shown in Figure 7a,b, while those of the GW and GW-H specimens are shown in Figure 7c,d. The images were obtained by stitching together sequential fractographs of the tested specimens.

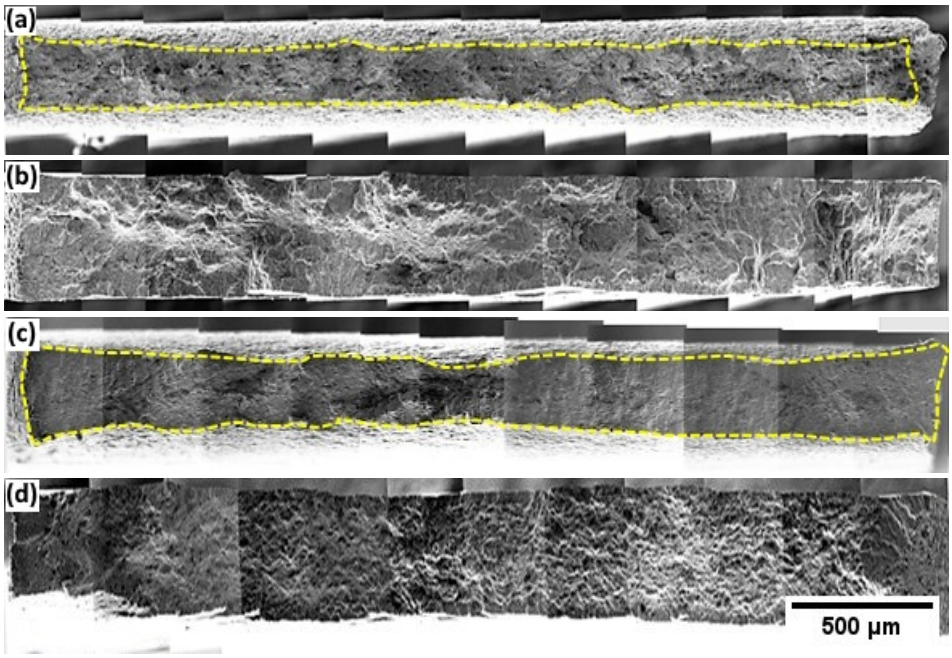

Figure 7. Fracture surfaces of specimens: (**a**) PW; (**b**) PW-H; (**c**) GW and (**d**) GW-H after tensile testing, taken from the mid-thickness of the pipe wall.

Failure of the PW specimen occurred in the HAZ, immediately adjacent to the BM region, while failure of the GW specimen occurred in the GW region. In both types of specimens, failure in the initial state proceeded via a mixed ductile–brittle mechanism, primarily through microvoid coalescence (MVC) and partially through quasi-cleavage (QC) (Figure 8a,b). "Necks" are observed in both types of specimens, indicating that they underwent plastic deformation before fracture. The neck of the specimen with the girth weld is narrower than that of the specimen with the production weld. The formation of brittle fracture zones (BFZs) in the PW and GW specimens is 10% and 5%, respectively, and is a result of the effect of natural gas during the service of the pipe.

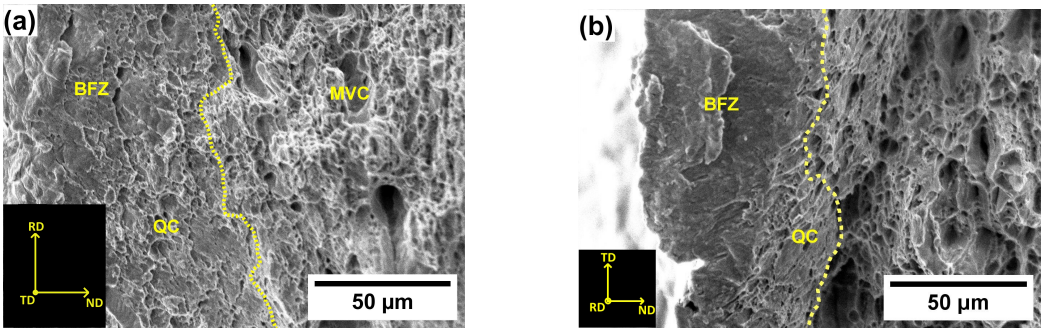

Figure 8. Fractures of PW (**a**) and GW (**b**) specimens taken from the mid-thickness of the pipe wall, showing clearly defined BFZ and ductile regions formed by MVC.

After additional hydrogen charging, the brittleness of the specimens increases sharply (Figure 7b,d. Evidence of this is the barely noticeable residual "neck" in the PW-H specimen and the absence of a neck in the GW-H specimen. The BFZs account for approximately 33.5% of the fracture surface in the PW-H specimen and about 57% in the GW-H specimen, which is around 3 and 11 times more in comparison to fractures of uncharged specimens. To quantitatively assess the degree of hydrogen embrittlement, the hydrogen embrittlement susceptibility (HES) indices of the tested specimens were calculated [32,33]:

$$HES = 1 - (\frac{f_H}{f}) \cdot 100\%, \quad (1)$$

where f_H and f are elongation ductility parameters measured in tensile tests after and before additional hydrogen charging, respectively. The calculated hydrogen embrittlement susceptibility indices, HES_{PW} = 42% and HES_{GW} = 52%. These results indicate that the specimens containing PW and GW are more prone to hydrogen embrittlement after hydrogen charging than uncharged PW and GW specimens respectively.

In the PW-H specimens, where the RD is perpendicular to the loading direction (LD), failure occurs in the BM adjacent to the HAZ and proceeds through the initiation and propagation of IC (Figure 9a) and transgranular (TG) (Figure 9a,b) cracks. The coalescence of these two types of cracks forms longitudinal cracks (LCs) oriented along the rolling direction (RD) (Figure 9a), reaching lengths of up to 150 µm and, in some areas, opening to 5–6 µm (Figure 9a). In the highlighted regions of Figure 9b, transgranular cracks developed along the ferrite–cementite grain boundaries of the pearlite are clearly visible. Their orientation is close to RD and thus aligns with the orientation of the ferrite and pearlite lamellae in the steel. This confirms the conclusions of our previous publication [27], indicating that pearlite–ferrite boundaries, or the interfaces between ferrite and cementite in lamellar pearlite, are preferred sites for hydrogen trapping.

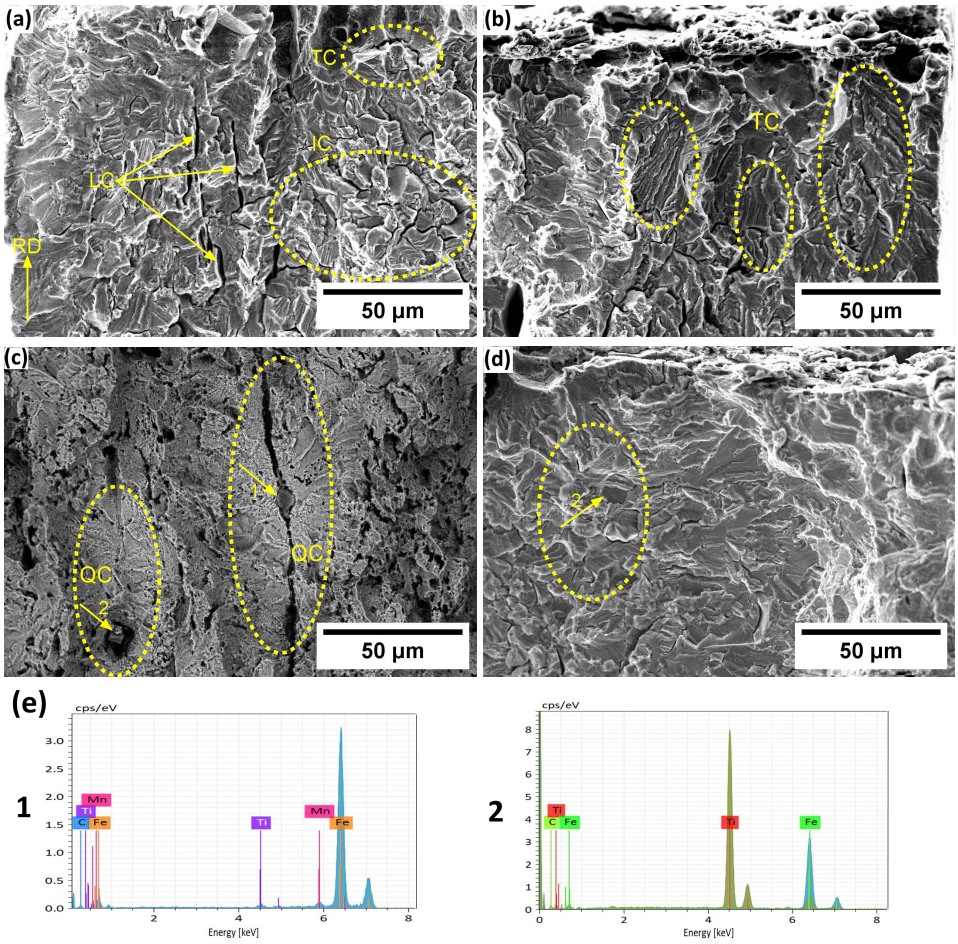

Figure 9. Fracture surface of specimen PW-H: (**a**) intergranular (IC) and longitudinal cracks (LC); (**b**) transgranular cracks (TC); (**c**) non-metallic inclusions—crack initiators; (**d**) non-metallic inclusion; (**e**) EDS spectra for the non-metallic inclusions (1) and (2), highlighted in the SEM micrograph in (**c**,**d**).

In the GW-H specimens, where the LD is parallel to the RD, fracture occurs entirely within the HAZ or in the weld seam. The dominant mechanism of brittle fracture is QC. The brittle fracture surface is mainly composed of the characteristic curved fracture facets typical of QC (Figure 10a,b). The fractographs reveal piercing features, which represent the outlets of cracks oriented perpendicular to the observation plane (Figure 10a,b).

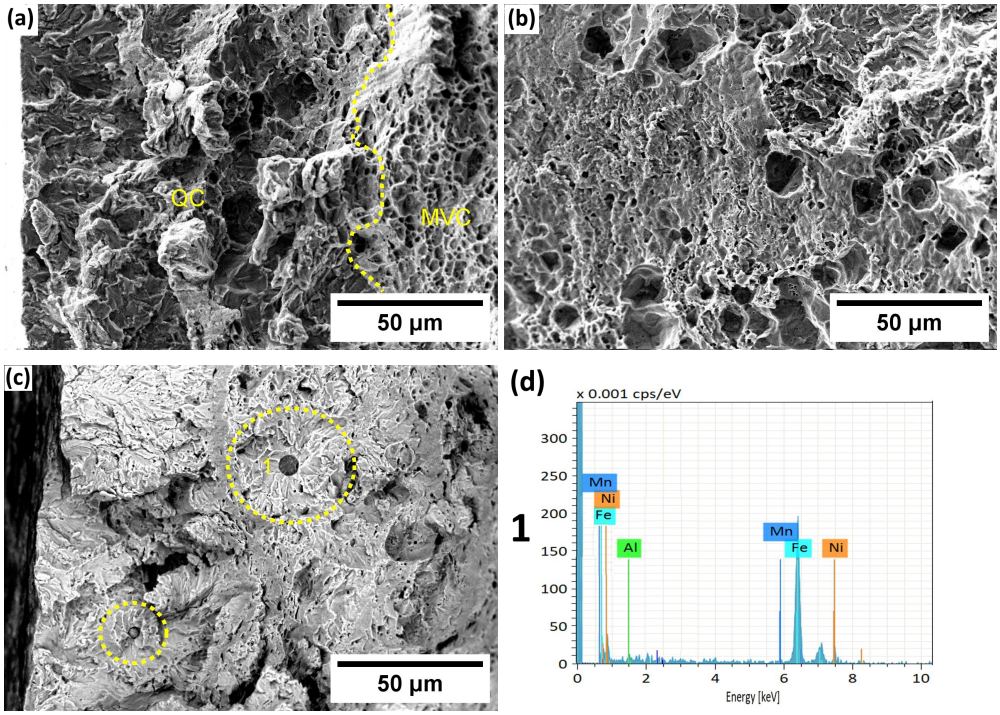

Figure 10. Fracture surface of specimen GW-H: (**a**) QC zone and MVC zone; (**b**) QC and crack penetration zone, perpendicular to the observation direction; (**c**) non-metallic inclusions—crack initiators (encircled by yellow circles); (**d**) EDS spectra for the non-metallic inclusion (1), highlighted in the SEM micrograph in (**c**).

As already discussed, fracture after tensile testing in the GW-H specimens occurred in the weld seam and the HAZ, where the microstructure is heterogeneous, consisting of a ferritic matrix, bainitic structures of complex morphology, and lamellar pearlite. The pearlitic microstructure has higher hardness and greater brittleness than the ferritic phase due to the larger number of interfaces. When a sufficient amount of hydrogen is present, cracks can develop both parallel and perpendicular to the cementite lamellae [27]. It is known that the interfaces of fine inter-lath cementite in the bainitic microstructure inhibit hydrogen diffusion [34], leading to hydrogen accumulation in these regions. This significantly reduces the fracture resistance.

Non-metallic inclusions play a significant role in the fracture of pipelines. During the welding process, various non-metallic inclusions of different composition and size precipitate in and near the weld seams. These inclusions act as crack initiators, while hydrogen further accelerates crack propagation [35,36]. In our study, in the PW-H specimens, non-metallic inclusions (compounds of Al, Ti, and Ni) are often arranged in chains along the RD. Their shape depends on the type of inclusion (Figure 9c,d), and longitudinal cracks almost always propagate directly adjacent to them or through them, in some cases even splitting the inclusions. In the GW-H specimens, the non-metallic inclusions are rounded and have partially or completely lost cohesion with the matrix (Figure 10c). QC zones form around them.

3.6. Microstructure Analysis

Figures 11 and 12 show typical microstructures of the production and girth welds, respectively, in the investigated low-carbon pipeline steel.

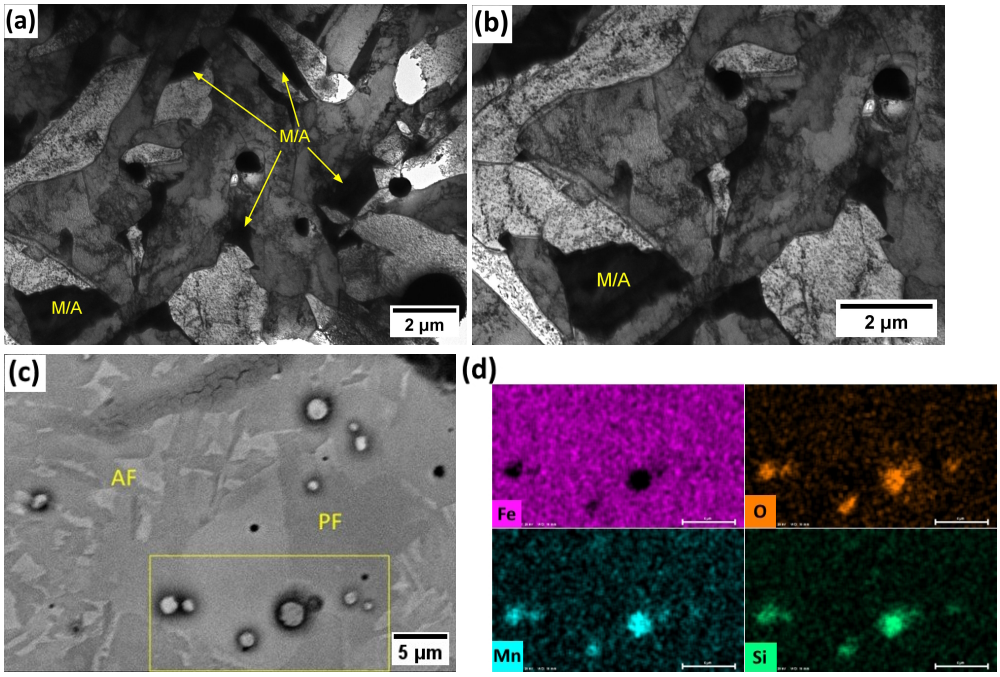

Figure 11. PW structure: (**a**,**b**) TEM images, presenting general microstructure and (**c**) SEM image and (**d**) the corresponding EDS analysis of the inclusions in it (EDS zone highlighted by yellow rectangle).

The microstructure of the weld seams consists mainly of AF and PF (Figures 11c and 12d). Acicular ferrite is considered an optimal microstructural constituent for improving impact toughness [1,37].

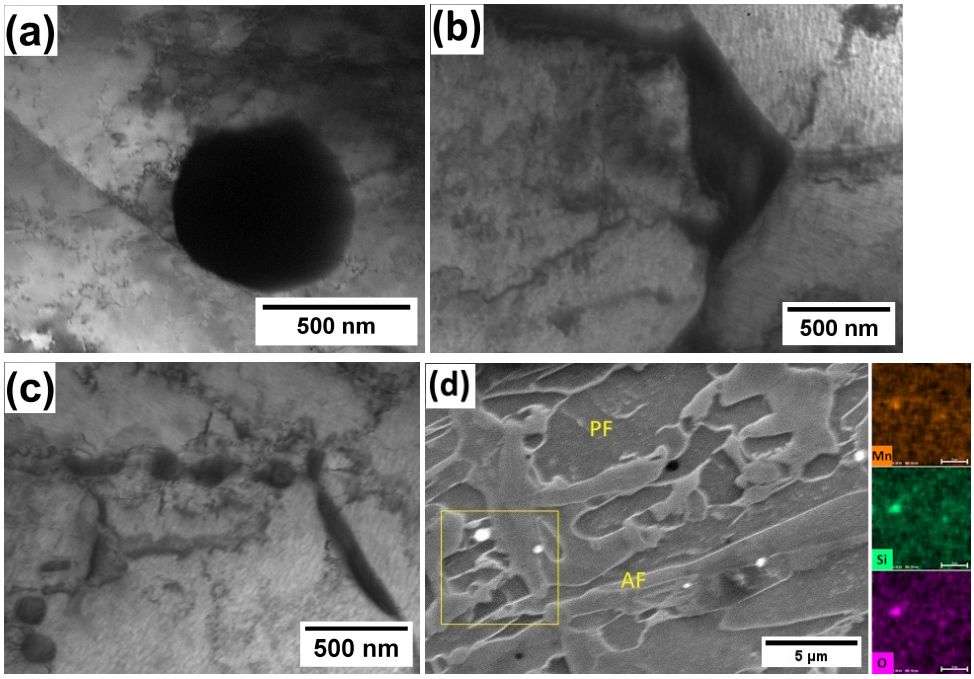

Figure 12. GW structure: TEM (**a**–**c**) and SEM **(d)** images with a corresponding EDS analysis of the inclusions in it (EDS zone highlighted by yellow rectangle). The scale bar of the EDS maps is 2 µm.

SEM and TEM observations further show that, in addition to acicular and polygonal ferrite, sub-micrometer spherical non-metallic inclusions are also present in the weld joint microstructure, most likely introduced during the welding process (Figures 11a,b and 12a). Elemental distribution analyses of the weld seams indicate that these non-metallic inclusions are primarily Si- and Mn-rich oxides (Figures 11c and 12d).

The non-metallic inclusions are enriched in Mn, which leads to the development of Mn-depleted zones in the matrix immediately surrounding the inclusions [1,37,38]. Such inclusions enhance the nucleation of acicular ferrite [1,37], while the Mn-depleted regions may act as hydrogen traps [38]. In the microstructure of the low-carbon steel, a blocky phase is also present along the ferrite grain boundaries (Figures 11a,b and 12b). Visually, this phase resembles the previously identified martensite/austenite (M/A) constituent in welded joint microstructures [1,39]. M/A constituents are metastable, and during welding, some of them decompose into ferrite and carbides distributed along ferrite grain boundaries. These carbides may exhibit either rod-like or rounded morphologies (Figure 12c) [1,39].

In the production weld seam, a larger number and greater size (0.5–2 μm) of non-metallic inclusions are observed compared to the girth weld seam (0.3–1 μm).

Figure 13 shows typical microstructures of the production and girth welds after hydrogen charging. The spherical non-metallic inclusions are incoherent with respect to the matrix [34,40], and around them a more pronounced electrochemically polished defective zone is observed (Figure 13). After hydrogen charging, the formation of a large number of dislocations in the ferrite grains is observed.

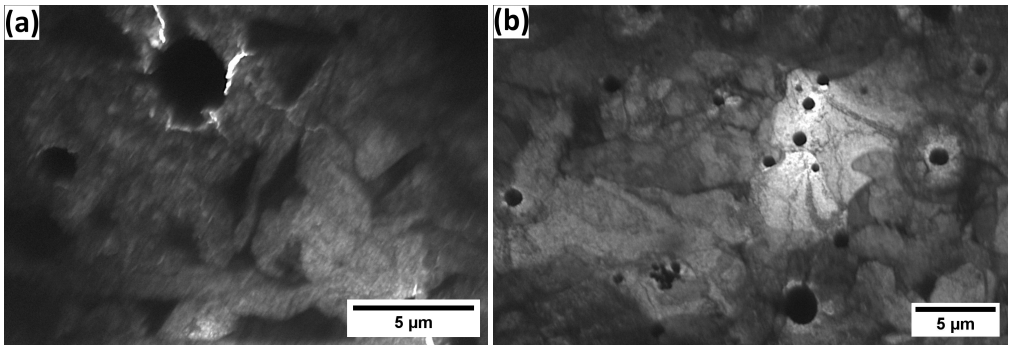

Figure 13. TEM images of the production (**a**) and girth (**b**) weld after additional hydrogen charging.

Figure 14 shows typical microstructures of the HAZ of the production and girth welds in the uncharged state, as well as after additional hydrogen charging. The microstructure consists of ferrite and pearlite (Figure 14a,c). TEM investigations did not reveal spherical non-metallic inclusions. Along the ferrite grain boundaries (Figure 14c), isolated rounded cementite particles are also observed. The dislocation structure is well developed within the ferrite. Hydrogen charging has led to the appearance of a higher density of dislocations in the HAZ regions of PW-H and GW-H (Figure 14b,d).

Pipeline steels, like all construction materials, contain non-metallic inclusions that change and evolve at different stages of production. These inclusions may differ in the weld metal, the HAZ, and the BM, depending on the manufacturing and welding technologies. The non-metallic inclusions shown in Figures 9d and 10d are located in the heat-affected zone and exhibit different compositions depending on the type of weld. The inclusions in the HAZ of PW are Ti-Mn compounds (Figure 9d). The composition of the inclusion located near GW is more complex and contains Mn, Ni, and Al (Figure 10d). This further confirms that the technologies used to produce these welded joints are different. The non-metallic inclusions shown in Figures 11c and 12d are located within the weld metal itself (PW and GW); they have a spherical shape and the same composition (Si, O, Mn). The formation of such inclusions in pipeline steels is typical both during production stages [40] and during

welding [1]. The considered non-metallic inclusions have a direct impact on the quality of the pipeline steel; they are incoherent with the matrix and may induce crack initiation, while the presence of hydrogen only increases this possibility.

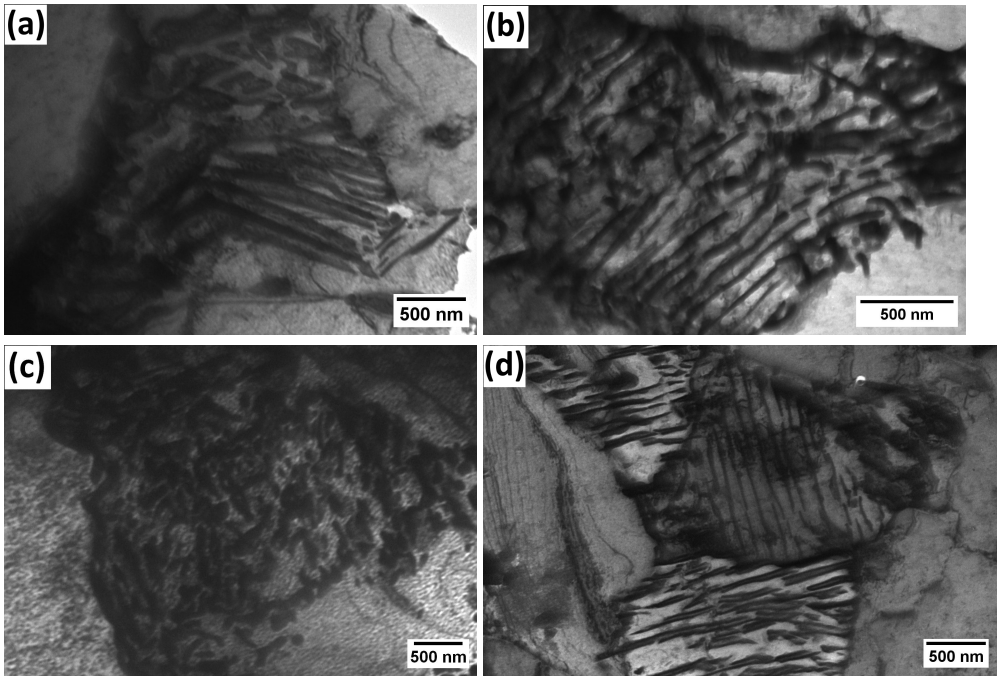

Figure 14. HAZ structure: TEM images of HAZ of PW (**a**,**b**) and GW (**c**,**d**) after long-term operation (**a**,**c**) and after additional hydrogen charging (**b**,**d**).

4. Conclusions

In this study, it was established that:

- Different pipeline regions (base material, production weld seam, and girth weld seam) exhibit distinct initial hydrogen contents, highlighting the strong influence of microstructure, defect density, and welding thermal cycles on hydrogen trapping capacity.
- After electrochemical charging, the hydrogen concentration ratios between regions change, indicating differing hydrogen accumulation behavior and variations in the type and density of hydrogen traps.
- Long-term service leads to region-specific hydrogen retention in the investigated pipeline steel, which can evolve under short-term charging or increased hydrogen levels, underscoring the critical role of structural heterogeneity in hydrogen embrittlement resistance and long-term pipeline reliability.
- In uncharged specimens, tensile failure localizes in the heat-affected zone, likely due to welding-induced stresses and carbon redistribution, which promote structural heterogeneity.
- Hydrogen charging alters the failure mode: damage extends from ferrite to pearlite, with pores, cracks, and microvoids consistent with HELP and HEDE mechanisms. Fracture occurs via intergranular/transgranular cracking in PW regions and quasi-cleavage in GW regions, while decohesion of non-metallic inclusions further promotes crack initiation.

In Part II of this study, the underlying mechanisms governing the observed hydrogen-related properties will be further investigated. Particular attention will be given to the characterization of the type and distribution of hydrogen traps in the three regions of the pipeline steel (base metal, girth weld, and production weld seams).

Author Contributions: Conceptualization, B.Y., V.D., R.L., K.V. and Y.M.; methodology, B.Y., V.D., K.V., Y.M., R.H.P. and R.K.; software, K.K.; validation, T.D., M.C. and B.Y.; formal analysis, Y.M., K.V., V.D., R.L., R.K. and T.S.; investigation, B.Y., K.V., Y.M., V.D., R.L., R.H.P., R.K., T.S., K.K., M.C. and T.D.; resources, K.K. and T.S.; data curation, R.L., R.H.P. and K.V.; writing—original draft preparation, K.K.; writing—review and editing, V.D., M.C., T.D. and R.H.P.; visualization, R.K.; supervision, R.L., V.D., K.V. and T.S.; project administration, R.L. and T.S.; funding acquisition, T.S. and R.L. All authors have read and agreed to the published version of the manuscript.

Funding: This research was financially supported by the National Recovery and Resilience Fund (RRF) of Bulgaria (Project PVU-51/BG-RRP-2.017-0022-C02).

Data Availability Statement: The original contributions presented in the study are included in the article; further inquiries can be directed to the corresponding author.

Acknowledgments: The work in this publication was performed using equipment funded by project BG16RFPR002-1.014-0006 "National Center for Mechatronics and Clean Technologies". We acknowledge Ivaylo Katzarov, Lyudmil Drenchev and Lyudmil Lyutov for the theoretical discussions that contributed to the improvement of this study.

Conflicts of Interest: The authors declare no conflicts of interest.

References

1. Qiao, G.Y.; Han, X.L.; Chen, X.W.; Wang, X.; Liao, B.; Xiao, F.R. Transformation of M/A constituents during tempering and its effects on impact toughness of weld metals for X80 hot bends. *Adv. Mater. Sci. Eng.* **2019**, *2019*, 6429045. [CrossRef]
2. Duan, R.; Wang, Y.; Luo, Z.; Wang, G.; Xie, G. Hydrogen embrittlement behavior in the nugget zone of friction stir welded X100 pipeline steel. *Int. J. Hydrogen Energy* **2023**, *48*, 8296–8309. [CrossRef]
3. Sun, Y.; Cheng, Y.F. Hydrogen permeation and distribution at a high-strength X80 steel weld under stressing conditions and the implication on pipeline failure. *Int. J. Hydrogen Energy* **2021**, *46*, 23100–23112. [CrossRef]
4. Li, J.; Wu, Z.; Zhu, L.; Zhang, Z.; Teng, L.; Zhang, L.; Lu, C.; Wang, R.; Zhang, C. Investigations of temperature effects on hydrogen diffusion and hydrogen embrittlement of X80 pipeline steel under electrochemical hydrogen charging environment. *Corros. Sci.* **2023**, *223*, 111460. [CrossRef]
5. Truschner, M.; Kroll, R.; Eichinger, M.; Keplinger, A.; Engelberg, D.L.; Mori, G. Hydrogen embrittlement characteristics in cold-drawn high-strength stainless steel wires. *Corros. Sci.* **2023**, *216*, 111109.
6. Zhao, W.; Du, T.; Li, X.; Sun, H.; Li, B.; Yuan, S. Effects of multiple welding thermal cycles on hydrogen permeation parameters of X80 steel. *Corros. Sci.* **2021**, *192*, 109797. [CrossRef]
7. *ASME B31.12-2023*; Hydrogen Piping and Pipelines. American Society of Mechanical Engineers: New York, NY, USA, 2024.
8. Mohtadi-Bonab, M.; Masoumi, M.; Szpunar, J. A comparative fracture analysis on as-received and electrochemically hydrogen charged API X60 and API X60SS pipeline steels subjected to tensile testing. *Eng. Fail. Anal.* **2021**, *129*, 105721. [CrossRef]
9. Song, J.; Curtin, W. Atomic mechanism and prediction of hydrogen embrittlement in iron. *Nat. Mater.* **2013**, *12*, 145–151. [CrossRef]
10. Koren, E.; Yamabe, J.; Lu, X.; Hagen, C.M.; Wang, D.; Johnsen, R. Hydrogen diffusivity in X65 pipeline steel: Desorption and permeation studies. *Int. J. Hydrogen Energy* **2024**, *61*, 1157–1169. [CrossRef]
11. *ISO 3183:2019*; Petroleum and Natural Gas Industries—Steel Pipe for Pipeline Transportation Systems. International Organization for Standardization: Geneva, Switzerland, 2019.
12. *ASME B31.8-2025*; Gas Transmission and Distribution Piping Systems. American Society of Mechanical Engineers: New York, NY, USA, 2025.
13. Qin, W.; Thomas, A.; Cheng, Z.; Gu, D.; Li, T.; Zhu, W.; Szpunar, J. Key factors affecting hydrogen trapping at the inclusions in steels: a combined study using microprint technique and theoretical modeling. *Corros. Sci.* **2022**, *200*, 110239. [CrossRef]
14. Izadi, H.; Tavakoli, M.; Moayed, M.H. Effect of thermomechanical processing on hydrogen permeation in API X70 pipeline steel. *Mater. Chem. Phys.* **2018**, *220*, 360–365. [CrossRef]
15. Wang, H.; Ming, H.; Wang, J.; Ke, W.; Han, E.H. Hydrogen permeation behavior at different positions in the normal direction of X42 and X52 pipeline steels. *Int. J. Hydrogen Energy* **2024**, *72*, 1105–1115. [CrossRef]
16. Ronevich, J.A.; Somerday, B.P.; San Marchi, C.W. Effects of microstructure banding on hydrogen assisted fatigue crack growth in X65 pipeline steels. *Int. J. Fatigue* **2016**, *82*, 497–504. [CrossRef]

17. Zhang, P.; Laleh, M.; Hughes, A.E.; Marceau, R.K.; Hilditch, T.; Tan, M.Y. A study on hydrogen embrittlement of a high-strength pipeline steel weldment after microstructure manipulation by targeted heat treatments. *Int. J. Hydrogen Energy* **2025**, *97*, 1199–1211. [CrossRef]
18. Du, Y.; Lv, L.; Chen, K.; Dang, G.; Xu, H.; Zheng, S. Investigating variations in hydrogen-assisted crack propagation of X52 pipeline steel with different microstructural characteristics. *Corros. Sci.* **2024**, *239*, 112417. [CrossRef]
19. Jiang, J.; Zeng, W.; Li, L. Effect of residual stress on hydrogen diffusion in thick butt-welded high-strength steel plates. *Metals* **2022**, *12*, 1074. [CrossRef]
20. Wang, Y.; Liu, Z.; Zhao, Q.; Zhang, H.; Zhen, Y.; Wu, G.; Cao, Y. Study on the effect of welding residual stress on hydrogen diffusion behavior in cracked pipeline girth welds. *Eng. Fail. Anal.* **2025**, *181* 109923. [CrossRef]
21. Oriani, R.A. The diffusion and trapping of hydrogen in steel. *Acta Metall.* **1970**, *18*, 147–157. [CrossRef]
22. Krom, A.H.; Koers, R.W.; Bakker, A. Hydrogen transport near a blunting crack tip. *J. Mech. Phys. Solids* **1999**, *47*, 971–992. [CrossRef]
23. Kumar, P.G.; Yu-ichi, K. Diffusible hydrogen in steel weldments. *Trans. JWRI* **2013**, *42*, 39–62.
24. Olden, V.; Alvaro, A.; Akselsen, O.M. Hydrogen diffusion and hydrogen influenced critical stress intensity in an API X70 pipeline steel welded joint–Experiments and FE simulations. *Int. J. Hydrogen Energy* **2012**, *37*, 11474–11486. [CrossRef]
25. Coetsee, T.; Mostert, R.J.; Pistorius, P.G.H.; Pistorius, P.C. The effect of flux chemistry on element transfer in Submerged Arc Welding: Application of thermochemical modelling. *J. Mater. Res. Technol.* **2021**, *11*, 2021–2036. [CrossRef]
26. Bai, J.; Zhang, M.; Ma, H.; Li, Z.; Mao, W.; Li, J.; Zhang, J. Investigation of hydrogen embrittlement in welded joints of the L360MH pipeline steel for hydrogen transportation. *Corros. Sci.* **2025**, *251*, 112940. [CrossRef]
27. Dyakova, V.; Yanachkov, B.; Valuiska, K.; Mourdjeva, Y.; Krastev, R.; Simeonova, T.; Kolev, K.; Lazarova, R.; Katzarov, I. The Impact of Hydrogen Charging Time on Microstructural Alterations in Pipeline Low-Carbon Ferrite–Pearlite Steel. *Metals* **2025**, *15*, 1079. [CrossRef]
28. Cauwels, M.; Depraetere, R.; De Waele, W.; Hertelé, S.; Depover, T.; Verbeken, K. Influence of electrochemical hydrogenation parameters on microstructures prone to hydrogen-induced cracking. *J. Nat. Gas Sci. Eng.* **2022**, *101*, 104533. [CrossRef]
29. Huang, H.; Zhang, Z.; Jin, X.; Zeng, Z.; Zhang, L.; Sun, J.; Ma, J.; Zhang, J. Microstructure and mechanical properties of low-carbon high-strength steel fabricated by submerged arc additive manufacturing. *Mater. Today Commun.* **2025**, *43*, 111796. [CrossRef]
30. Oh, D.K.; Hwang, B. Hydrogen embrittlement of ferrite-pearlite OCTG steels under electrochemical and gaseous hydrogen environment. *J. Mater. Res. Technol.* **2025**, *37*, 3822–3831. [CrossRef]
31. Jiang, Y.; Zhang, B.; Wang, D.; Zhou, Y.; Wang, J.; Han, E.H.; Ke, W. Hydrogen-assisted fracture features of a high strength ferrite-pearlite steel. *J. Mater. Sci. Technol.* **2019**, *35*, 1081–1087. [CrossRef]
32. Zvirko, O.; Nykyforchyn, H.; Krechkovska, H.; Tsyrulnyk, O.; Hredil, M.; Venhryniuk, O.; Tsybailo, I. Evaluating hydrogen embrittlement susceptibility of operated natural gas pipeline steel intended for hydrogen service. *Eng. Fail. Anal.* **2024**, *163*, 108472. [CrossRef]
33. Konert, F.; Campari, A.; Nietzke, J.; Sobol, O.; Paltrinieri, N.; Alvaro, A. Evaluation of the tensile properties of X65 pipeline steel in compressed gaseous hydrogen using hollow specimens. *Procedia Struct. Integr.* **2024**, *54*, 204–211. [CrossRef]
34. Mohtadi-Bonab, M.; Masoumi, M. Different aspects of hydrogen diffusion behavior in pipeline steel. *J. Mater. Res. Technol.* **2023**, *24*, 4762–4783. [CrossRef]
35. Mohtadi-Bonab, M.; Eskandari, M. A focus on different factors affecting hydrogen induced cracking in oil and natural gas pipeline steel. *Eng. Fail. Anal.* **2017**, *79*, 351–360. [CrossRef]
36. Laureys, A.; Depraetere, R.; Cauwels, M.; Depover, T.; Hertelé, S.; Verbeken, K. Use of existing steel pipeline infrastructure for gaseous hydrogen storage and transport: A review of factors affecting hydrogen induced degradation. *J. Nat. Gas Sci. Eng.* **2022**, *101*, 104534. [CrossRef]
37. Qi, X.; Wang, X.; Di, H.; Shen, X.; Liu, Z.; Huan, P.; Chen, L. Effect of Ti content on the inclusions, microstructure and fracture mechanism of X100 pipeline steel laser-MAG hybrid welds. *Mater. Sci. Eng. A* **2022**, *831*, 142207. [CrossRef]
38. Wang, B.; Liu, X.; Wang, G. Inclusion characteristics and acicular ferrite nucleation in Ti-containing weld metals of X70 pipeline steel. *Steel Res. Int.* **2018**, *89*, 1700316. [CrossRef]
39. Xie, X.; Sun, J. Microstructure and mechanical property of 738 low alloy steel welded joint. *Heat Treat. Surf. Eng.* **2019**, *1*, 115–122. [CrossRef]
40. Zhu, H.; Zhao, J.; Li, J.; Hu, Q.; Peng, C. Evolution of nonmetallic inclusions in pipeline steel during LF and VD refining process. *High Temp. Mater. Processes* **2020**, *39*, 424–432. [CrossRef]

Disclaimer/Publisher's Note: The statements, opinions and data contained in all publications are solely those of the individual author(s) and contributor(s) and not of MDPI and/or the editor(s). MDPI and/or the editor(s) disclaim responsibility for any injury to people or property resulting from any ideas, methods, instructions or products referred to in the content.